J. Fluid Mech. (1989), *vol.* 199, *pp.* 471–494
Printed in Great Britain

Surface wave mode interactions: effects of symmetry and degeneracy

By F. SIMONELLI AND J. P. GOLLUB
Physics Department, Haverford College, Haverford, PA 19041, USA *and*
Physics Department, The University of Pennsylvania, Philadelphia, PA 19104, USA

(Received 15 March 1988)

Parametrically excited surface wave modes on a fluid layer driven by vertical forcing can interact with each other when more than one spatial mode is excited. We have investigated the dynamics of the interaction of two modes that are degenerate in a square layer, but non-degenerate in a rectangular one. Novel experimental techniques were developed for this purpose, including the real-time measurement of all relevant slowly varying mode amplitudes, investigation of the phase-space structure by means of transient studies starting from a variety of initial conditions, and automated determination of stability boundaries as a function of driving amplitude and frequency. These methods allowed both stable and unstable fixed points (sinks, sources, and saddles) to be determined, and the nature of the bifurcation sequences to be clearly established. In most of the dynamical regimes, multiple attractors and repellers (up to 16) were found, including both pure and mixed modes. We found that the symmetry of the fluid cell has dramatic effects on the dynamics. The fully degenerate case (square cell) yields no time-dependent patterns, and is qualitatively understood in terms of third-order amplitude equations whose basic structure follows from symmetry arguments. In a slightly rectangular cell, where the two modes are separated in frequency by a small amount (about 1%), mode competition produces both periodic and chaotic states organized around unstable pure and mixed-state fixed points.

1. Introduction

When a fluid layer is subjected to a uniform oscillation, standing waves at half the driving frequency occur as the result of a parametric instability first observed by Faraday. The interaction between surface wave modes leads to a variety of interesting nonlinear phenomena, including chaotic dynamics. Modal interaction generally occurs when two modes are simultaneously resonant or nearly resonant. Various authors have addressed aspects of this problem.

Miles (1976) investigated nonlinear surface waves by first treating the inviscid problem using Hamiltonian methods, and then adding linear damping to account for the dissipation found in experimental systems. Later, Miles (1984*a*) analysed in detail the dynamics of two modes with natural frequencies in the ratio 1:2 interacting in a cylindrical container subjected to vertical oscillation. The problem of modal interactions in a cylindrical container subjected to horizontal excitation was also analysed (Miles 1984*b*), and has recently been addressed experimentally by Funakoshi & Inque (1987), who found generally good agreement with the theoretical predictions.

Several years ago, Ciliberto & Gollub (1984, 1985*a*, *b*) studied the competition of

two modes with a ratio of natural frequencies close to unity, in a cylindrical container subjected to vertical excitation. They found that chaotic states occur as a result of spatial mode competition. Meron & Procaccia (1986*a*, *b*) subsequently derived a set of amplitude equations for comparison to these experiments, and succeeded in explaining the major experimental observations. Holmes (1986), using a perturbation technique originally due to Melnikov, demonstrated the existence of chaos for the interaction of two or more spatial modes in a vertically excited container. Gu & Sethna (1987) analysed in detail the problem of interactions between modes with frequency ratio 1:2 in a rectangular geometry.

In all of these investigations, the existence of a resonance condition between two modes is crucial to the dynamical behaviour. The effect of modifying the internal detuning (natural frequency difference) of the two modes has not yet been addressed experimentally. In the present paper, we report an experimental investigation of modal interactions in the square and rectangular geometry. Our attention is concentrated on pairs of modes that are degenerate in a square cell and non-degenerate when the symmetry is broken. The major goal of the investigation is to understand the consequences of symmetry and degeneracy in modal interactions. The significance of this effort is not limited to surface waves or even fluid systems. In fact, the form of the dynamical equations for the slowly varying mode amplitudes is expected to be determined by symmetry considerations combined with normal form analysis, without detailed computations (Meron 1987). On the other hand, amplitude equations determined by perturbation analysis of the hydrodynamic equations are certainly required for quantitative comparison, and full numerical computations based on the partial differential equations may be required in some cases. These experiments may shed light on the relative merits of these different theoretical approaches.

From an experimental point of view, the problem of studying modal interactions is not an easy one. Even if only two spatial modes contribute significantly to the dynamics, four slowly varying amplitudes must be measured to specify the state of the interface. Furthermore, the bifurcation structure of the problem is not completely determined by the stable states of the system: one would like to study the basins of attraction and detect the unstable fixed points as well. Finally, several different parameters must be adjusted to map out the behaviour of the system (including driving amplitude and driving frequency). Since the bifurcation structure is complicated, and small changes in these parameters are quite significant, automated methods of finding stability boundaries experimentally are required. Various experimental innovations allowed these requirements to be met.

2. Theoretical background

2.1. *Single-mode dynamics*

The surface deformation produced by each spatial mode in rectangular geometry has the form

$$Z_{mn}(x,y,t) = [A_{mn}(t)\cos(\tfrac{1}{2}\omega t) + B_{mn}(t)\sin(\tfrac{1}{2}\omega t)]\,[\cos(m\pi x/L_x)\cos(n\pi y/L_y)]. \quad (2.1)$$

Here $\omega = 2\pi f$ is the driving angular frequency, A_{mn} and B_{mn} are mode amplitudes that in the weakly nonlinear regime vary on a timescale much larger than $1/\omega$, m and n are integers giving the number of half-wavelengths in the x- and y-directions, and L_x and L_y are the dimensions of the cell containing the fluid.

The dynamics can be reduced to a set of amplitude equations, that is, ordinary differential equations in the slowly varying mode amplitudes. The dynamical behaviour of a single spatial mode is described in a two-dimensional phase space for the in- and out-of-phase amplitudes. Amplitude equations appropriate for this case were derived by Miles (1984*a*) and later by Gu, Sethna & Narain (1988); these latter authors included a detailed analysis for the specific case of rectangular geometry. The basic approach was to perform a perturbation analysis (limited to third order in the amplitudes) of the partial differential equations for the inviscid problem. Linear damping was then added to account for the dissipation present in a real system (Miles 1967). The resulting equations have the form

$$\dot{C}_{mn} = \alpha C_{mn} + \beta \bar{C}_{mn} + \gamma |C_{mn}|^2 C_{mn} = S(C_{mn}, \bar{C}_{mn}), \tag{2.2}$$

where the complex amplitude $C_{mn} = A_{mn} - \mathrm{i}B_{mn}$, and the right-hand side will be later abbreviated as a function S of the complex amplitudes.

The asymptotic states correspond to either the flat surface or two standing waves. However, several interesting predictions concerning unstable solutions and transient behaviour were obtained from analytical and numerical analysis of those equations (Gu *et al.* 1988). The onset of waves was predicted to be subcritical (with hysteresis) for $f < 2f_{mn}$ (where f_{mn} is the natural frequency of the mode) and supercritical for $f > 2f_{mn}$. The basins of attractions of the various fixed points are expected to be interlaced as they spiral out from the neighbourhood of the origin. Those predictions as well as the experimental verification of some of them are further discussed in §4. (Some measurements on a single mode were performed by Virnig, Berman & Sethna 1988. The prediction of hysteresis also follows from simple considerations involving amplitude equations, as discussed by Meron 1987.)

2.2. *Interacting modes*

When two or more spatial modes are excited simultaneously, the amplitude equations contain the independent dynamics of each of the modes and also their coupling. For general boundary conditions, the coupling can be quite complex. On the other hand, symmetry considerations greatly simplify the task of obtaining the amplitude equations by reducing the number of allowed coupling terms at any given order in the perturbation expansion. The form of the equations can be obtained even if the calculations are not performed explicitly (Meron 1987; J. Guckenheimer 1988, private communication; Golubitsky & Shaffer 1985). In the following, we briefly discuss the form of the appropriate amplitude equations for the square and rectangular geometry.

The equations must be invariant under a simultaneous change of sign of the amplitudes (A_{mn} and B_{mn}) of all the modes. This is because a translation in time equal to one period of the forcing leaves the physical system unaffected. Such a translation corresponds to a phase shift of all the modes by π with respect to the forcing, since they oscillate at half the driving frequency. Such a phase shift is of course equivalent to a sign change of A_{mn} and B_{mn}.

If the cell has rectangular symmetry, the group of transformation that leave the system invariant can be generated by two reflections through planes parallel to the x- and y-axes. We will call those reflections R_x and R_y, respectively. A given spatial mode will be either antisymmetric or symmetric for each of those reflections, meaning that the corresponding Z_{mn} will change sign or remain the same, respectively. In particular the modes (m, n) for which m (or n) is odd are antisymmetric under R_x (*or* R_y). The signs of the corresponding amplitudes are

changed in (2.1) when the transformation is applied, but the invariance of the physical system implies that the amplitude equations must not change (Meron & Procaccia 1986*b*; Simonelli & Gollub 1987). Finally, in the limiting case of square geometry certain pairs of completely degenerate modes transform into each other under a 90° spatial rotation. As a consequence, the amplitude equations must also be invariant under an exchange of the amplitudes of such symmetry-related modes.

From the general treatment of parametrically forced systems (Meron 1987), it is possible to limit further the number of terms in the equations by the elimination of all of the terms that are 'non-resonant' with the forcing, thus reducing the system to its 'normal form' (Guckenheimer & Holmes 1983; Meron & Procaccia 1986*b*).

The experiments described in the subsequent sections are mostly concerned with the two modes (3, 2) and (2, 3) in rectangular and square geometry. For those two modes the equations (up to cubic order) would read

$$\left.\begin{aligned}\dot{C}_{32} &= S_{32}(C_{32}, \bar{C}_{32}) + \mu_{32} C_{32} |C_{23}|^2 + \nu_{32} \bar{C}_{32} C_{23}^2, \\ \dot{C}_{23} &= S_{23}(C_{23}, \bar{C}_{23}) + \mu_{23} C_{23} |C_{32}|^2 + \nu_{23} \bar{C}_{23} C_{32}^2.\end{aligned}\right\} \tag{2.3}$$

where the function S, containing the single-mode dynamics, was defined by equation (2.2), and the other terms in each equations are the only allowed coupling terms. (For example, a term such as $\bar{C}_{32} C_{23}^2$ cannot be present in the lower equation because the R_y symmetry requires invariance of the equation under a sign change of C_{23} only.) In the degenerate case of a square cell, the corresponding coefficients are identical and the two equations will then be interchangeable. Thus, symmetry requirements and the resonance condition are sufficient to specify the form of the amplitude equations.

The invariance requirements due to symmetry translate into equivalent requirements for the structure of the phase space (attractors, basins of attraction, unstable solution, etc). This means that for each fixed point there will be others related to it by symmetry transformations. These considerations may be applied directly to experimental data without any other theoretical assumptions, and on several occasions were of great help in determining the bifurcation structure of the system.

3. Experimental set-up

The experiments were performed in containers with typical horizontal sizes of 6 cm and a depth of 2.5 cm. We used n-butyl alcohol because it was found to give a uniform contact line at the Plexiglas walls. The vertical oscillation was provided by an electromagnetic shaker (Vibration Test Systems model 40C) driven by a synthesizer (Hewlett Packard model 3325A) and a high-quality power amplifier. The vertical acceleration (and consequently the drive amplitude) was measured with an accelerometer (Dytran model 3134A).

The experimental methods employed here to study surface waves have been described in detail elsewhere (Simonelli & Gollub 1988). Therefore, we limit our discussion of experimental techniques to essential matters. Basically, there are three *novel* features to the methods employed in this work: (*a*) all of the significant mode amplitudes were measured; (*b*) the stability boundaries were determined in an automated fashion; and (*c*) the transients and basins of attraction were studied in addition to the attractors themselves.

3.1 *Modal decomposition*

The experimental methods were inspired by the need to measure all of the slowly varying amplitudes A_{mn} and B_{mn} contributing to the deformation field $Z(x, y, t)$. These amplitudes can be measured by utilizing a number of local probes equal to the number of nearly resonant modes. The output of each probe is sent to a double-phase lock-in amplifier, which produces signals proportional to the in- and out-of-phase components of the surface displacement at that location. Since the spatial distribution of the modes and the locations of the probes are known, a simple linear combination of the signals from the various probes yields the individual mode amplitudes A_{mn} and B_{mn}. (For the case of two modes, there are two probes and four mode amplitudes.)

The local probes actually employed are photodiodes sensitive to the optical intensity in a shadowgraph image. In figure 1 (*a*, *b*) we show two examples of images formed by surface wave patterns relevant to the present paper. Local probes based on such images have the advantage of not being intrusive. Though some nonlinearity is present in the shadowgraph image if the wave height is not small compared with the wavelength, this is not a serious problem for the present investigation because the most important experimental quantities are ratios of the mode amplitudes. The measurement nonlinearity was found to yield errors of only a few per cent in these ratios. However, the errors in the individual amplitudes due to optical nonlinearity can be up to 25% in some cases. If desired, non-optical probes could be utilized, but these have the disadvantage of possibly perturbing the flow.

3.2. *Parameter-space structure*

There are two essential parameters that affect the dynamics: the driving frequency $f = \omega/2\pi$, and driving amplitude Δ. Since the dynamics are extremely sensitive to these quantities, we found it useful to use an automated scanning process to locate the stability boundaries by a method of successive approximation. In searching for the stability boundaries of the flat surface state, for example, the computer scans the amplitude Δ at constant driving frequency, alternatively with positive and negative increments (to allow for possible hysteresis). As the search converges, the step size is reduced and the waiting time between steps is increased. The trade-off between time and accuracy has been discussed by Simonelli & Gollub (1988). The computer search is stopped and another driving frequency is chosen when the desired accuracy is attained.

3.3. *Phase-space structure and transients*

We explored the structure of the phase space by means of a large number of transients starting from a variety of initial conditions. This was accomplished by starting from parameters (f', Δ') deviating slightly from the point (f, Δ) under investigation, and then switching the parameters to (f, Δ) suddenly. In some cases, the phase of the driving was also stepped to obtain initial conditions not otherwise accessible. This approach gives the possibility of following the stable and unstable fixed points, and the structure of the basins of attraction in phase space, as a function of f and Δ.

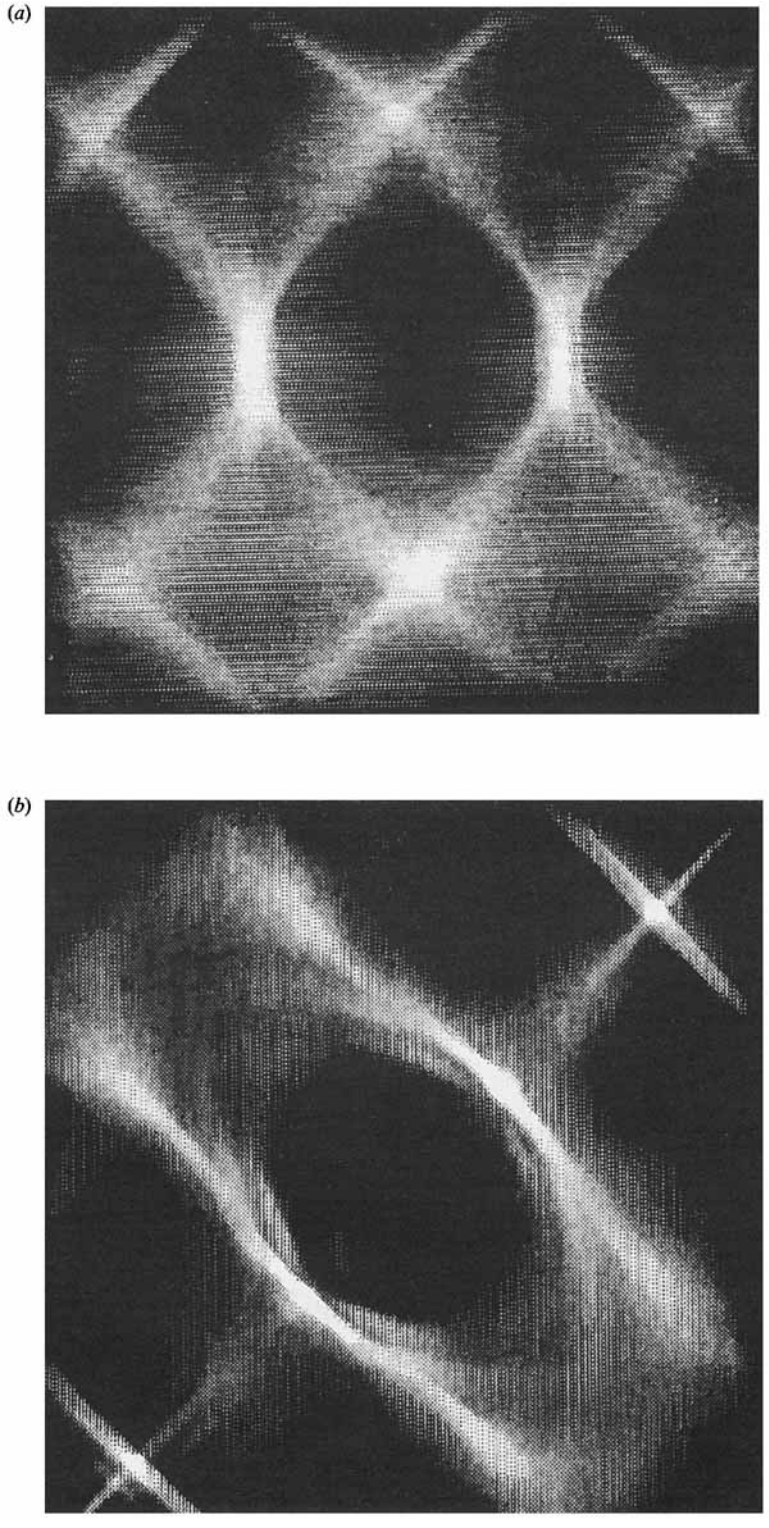

FIGURE 1. Shadowgraph images produced by (*a*) a pure (3, 2) mode and (*b*) a superposition of the (3, 2) and (2, 3) modes with equal amplitudes. The images have been averaged over one period of the forcing and then digitally enhanced.

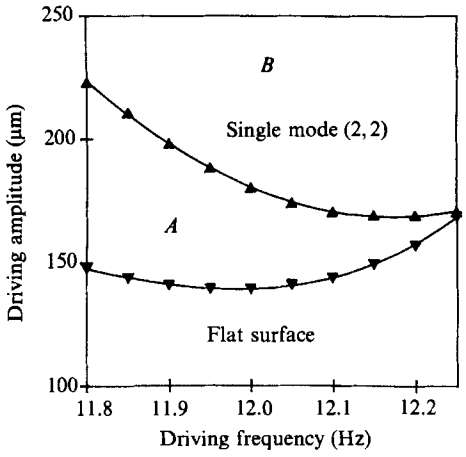

FIGURE 2. Experimental parameter space for the (2,2) spatial mode in a square cell. Stability boundaries are shown as a function of driving amplitude Δ and frequency f. The wave onset is subcritical for $f < 2f_{22} = 12.24$ Hz, where f_{22} is the natural frequency of the mode. The hysteretic region A shrinks to zero at the resonant frequency. In this and subsequent figures, the driving amplitude may be compared to the half-wavelength, which is typically 2 cm.

4. Single-mode dynamics

To study the single-mode dynamics, we concentrated on the (2, 2) mode in a square cell. An experimental parameter-space diagram obtained by automated scanning is shown in figure 2. (We have chosen to use physical units rather than dimensionless variables in presenting the results, to preserve a sense of the actual scale of the phenomena.) The two curves represent the thresholds for the waves upon increasing and decreasing Δ. Hysteresis is clearly visible for $f < 2f_{22}$, and the hysteretic interval goes to zero approximately at the resonance, as predicted. (Gu *et al.* 1988 actually predict that the transition from inverted to normal bifurcation occurs for a slightly positive detuning. This small correction would not be visible with the accuracy of the threshold measurements allowed by our apparatus.) Unfortunately, the onset of the (3,0) and (0,3) modes prevents study of the region $f < 2f_{22}$.

Three distinct regions are found in figure 2. At the lowest Δ only the flat surface is stable. In region A the flat-surface state and two stationary waves, differing by π in the phase $\phi_{22} = \arctan(-B_{22}/A_{22})$, coexist for a total of three stable fixed points. Finally, in region B the stable states are the two stationary waves.

The transition at the lower boundary of region A is predicted to occur via two simultaneous saddle-node bifurcations. We represent this process by the schematic notation $\mathrm{Si} \rightarrow \mathrm{Si} + 2(\mathrm{Sa} + \mathrm{Si})$, where Si represents a sink and Sa is a saddle. (The introduction of this notation is unnecessary here, but is useful in the more complex case of modal interactions to follow.) At the upper edge of region A, the saddles merge with the origin, which then loses its stability: $\mathrm{Si} + 2\mathrm{Sa} \rightarrow \mathrm{Sa}$.

The predicted phase-space structure is quite interesting, especially in region A where the flat surface and stationary waves coexist. The various basins of attraction are expected to be interlaced in such a way that, for example, it is possible to reach the origin starting with a wave of arbitrary amplitude, provided that the initial phase ϕ is appropriate. In figure 3(*a*), we reproduce the corresponding phase-space diagram from Gu *et al.* (1988); it shows the basins of attraction of the various fixed points.

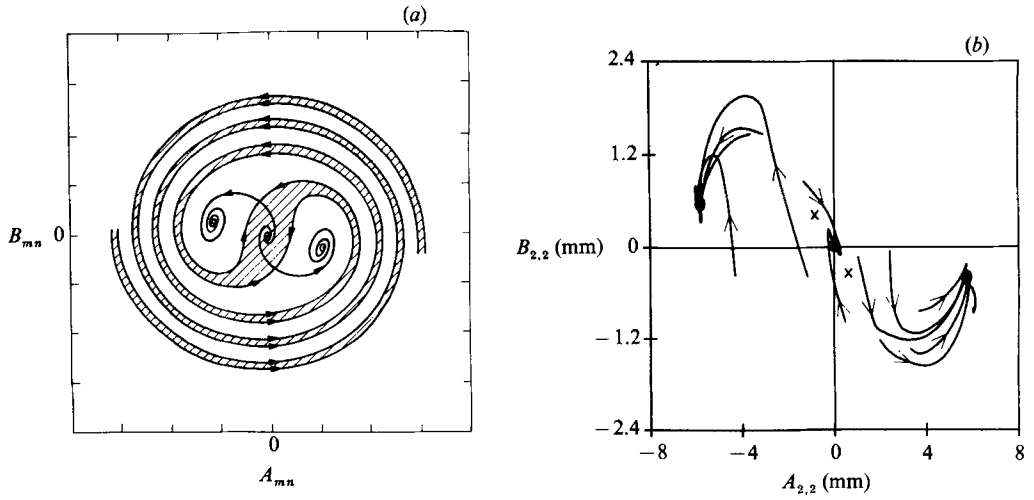

FIGURE 3. Theoretical and experimental phase diagrams for a single spatial mode, corresponding to region A of figure 1. (a) Theoretical phase-space structure, reproduced from Gu *et al.* (1988). The diagram contains two symmetric fixed points corresponding to stationary waves, the fixed point at the origin, and two saddles. The basins of attraction of these fixed points are interlaced. (b) Experimental phase space showing essentially the same structure as in (a). The approximate locations of the saddles are shown by the symbol ×. In this and subsequent figures, the wave amplitudes may be compared to the half-wavelength, which is typically 2 cm.

Using controlled initial conditions, we were able to observe this behaviour qualitatively, as shown in figure 3(b). Three stable fixed points corresponding to the flat surface and to stationary waves are clearly visible. From the transients leading to the origin it is clear that this state can be reached starting with a larger wave than some initial conditions leading to stationary wave states, provided the initial phase is appropriate. It is apparent that there must be saddle points also, but we were unable to determine their location accurately with the limited number of transients shown. It is difficult to study the single-mode dynamics quantitatively because damping causes the timescale of the transients to be relatively fast. They last only a few wave periods, owing to the small size of the system. The comparison between figures 3(a) and 3(b) can be made only at the qualitative level because the parameters do not correspond in the two cases.

5. Interaction of completely degenerate modes in square symmetry

To study the interaction of two completely degenerate modes, we used a square cell of size 6.17 cm. Attention was concentrated on the modes (3, 2) and (2, 3), because they are adequately separated from other resonances. In addition, symmetry considerations provide stronger constraints on the form of the dynamical equations for this pair of modes than for some others, since one of the indices is odd, and the other is even, as discussed in §2.

5.1. *Parameter-space diagram*

In figure 4(a), we present an experimental parameter-space diagram showing the major resonance of interest and the neighbouring ones. The hysteresis described in §4 for isolated modes is present here as well. In figure 4(b), the structure near the (3, 2)–(2, 3) resonance is shown in much greater detail, including additional stability

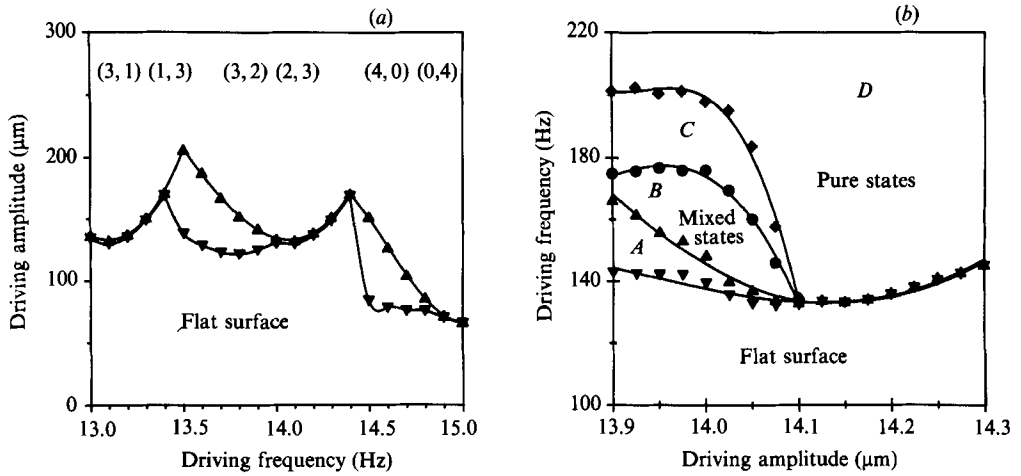

FIGURE 4. (*a*) Parameter-space diagram for a square cell (6.17 × 6.17 cm). Several resonances are visible, corresponding to pairs of distinct but degenerate modes. The resonances are asymmetric: subcritical on the left, and supercritical on the right. (*b*) Expanded view near the (3,2)–(2,3) resonance. Three primary regions are found: the flat surface, mixed states in region *B*, and pure states in region *D*. The intermediate regions *A* and *C* are characterized by coexistence of different types of fixed points (flat or mixed in *A*, mixed or pure in *C*) which are realized for different initial conditions.

boundaries. There is of course a region in which only the flat surface is stable. In region *B* of the diagram the stable states are superpositions of the two modes, with equal amplitudes ($|C_{32}|^2 = C_{23}|^2$). Owing to the symmetry properties of these modes under the transformations R_x and R_y, four equivalent mixed states are expected and are found experimentally. In two of them the phase difference $\delta\phi$ between the two modes is zero, while for the other two $\delta\phi = \pi$. In region *D*, on the other hand, only pure states are found. Owing to the symmetry, either pure state can be found depending on the initial conditions. Regions *A* and *C* are hysteretic: in *A* the flat-surface state coexists with mixed states, while in *C* mixed states coexist with pure states. Examples of shadowgraphs produced by a pure (3,2) state and an in-phase mixed state are shown in figure 1. (The apparently large harmonic content of the images is due to optical nonlinearity and image enhancement.)

The range of frequencies in the parameter-space diagram is limited by the need to avoid excitation of other modes. The range in Δ is limited by the occurrence of more complicated phenomena caused by strong nonlinearity. For example, when Δ is increased above the values represented in the diagram, breaking of the waves occurs. The study of such states is outside the domain of this paper.

Qualitative observations were performed on other pairs of degenerate modes. For the (3,1)–(1,3) resonance, mixed states and pure states were also found, and the parameter-space structure is similar to the one just described for the (3,2)–(2,3) resonance. However, there are some differences. The modes (3,1) and (1,3) both change sign under either R_x or R_y; hence reflection symmetries do not simplify the amplitude equations in this case, so the existence of mixed states with $\delta\phi = 0$ does not imply the existence of mixed states with $\delta\phi = \pi$ and vice versa. In fact, only $\delta\phi = 0$ was observed. Similarly, reflection symmetries do not constrain the (4,0)–(0,4) modal interactions (because these modes are invariant under both R_x and R_y) and we observed only $\delta\phi = \pi$ for this case. The excitation of other nearby modes prevented a thorough investigation of these resonances.

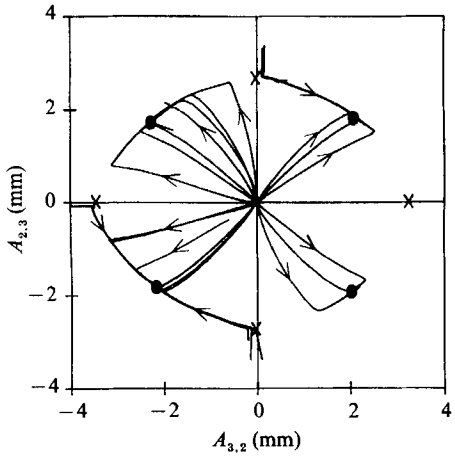

FIGURE 5.

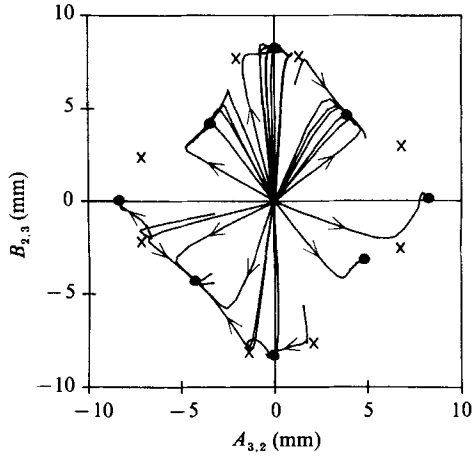

FIGURE 6.

FIGURE 5. Experimental phase-space diagram in region B, showing a bidimensional projection in the plane of the in-phase amplitudes. About thirty transients are shown in the diagram, most of which start in the vicinity of the origin. Four symmetric mixed states are visible. Observation of the trajectories near the axes shows that the four pure states are saddles.

FIGURE 6. Experimental phase-space diagram in region C. Four mixed and four pure states are stable in his region, as revealed by the asymptotic behaviour of the trajectories. Eight saddles (×) are located between them. The distances of the various fixed points from the origin are comparable but not identical.

5.2. *Bifurcations of fixed points*

Using the method of controlled initial conditions, we have been able to map out the basic phase-space structure corresponding to each of the regions of parameter space. We present two examples in figures 5 and 6, corresponding respectively to regions B and C of figure 4(b). (The diagrams are two-dimensional projections on the subspace of the in-phase amplitudes.) A careful examination of these figures reveals the locations of the stable and unstable fixed points, which are denoted by solid circles and crosses. The expected reflection and rotation symmetries are visible even with a relatively limited number of trajectories.

At this point, we turn from the actual experimental data to *schematic* phase-space diagrams (figure 7) showing the structure for the various regions of the parameter space, using a similar projection. The geometry has been simplified to show the essential features. In region A both the flat-surface and mixed states are stable and are reached for different initial conditions. The phase space is organized around sinks located at the origin and symmetrically along 45° lines; these latter are mixed states. Four pure-state fixed points are also shown by a cross, but these are unstable (saddles). We infer from a combination of direct experimental evidence and the following theoretical considerations that there must be eight additional fixed points, located on an inner ring, four of which are mixed-state saddles and four of which are pure-state sources (open circles).

As pointed out in §2, the amplitude equations for two interacting spatial modes contain the single-mode terms plus nonlinear coupling terms. The existence and locations of the pure-state fixed points are unaffected by the coupling, because the cross-terms vanish when one of the mode amplitudes is zero. (However, the stability properties of these fixed points may be and, in fact, are affected by the coupling.) From this consideration, it is clear that the number of pure-state solutions must be

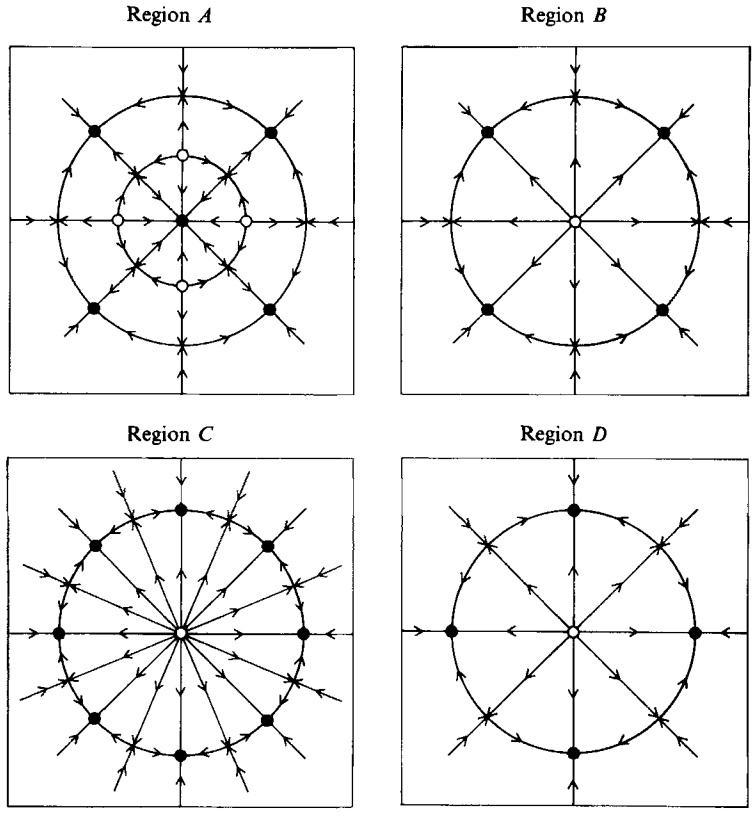

FIGURE 7. Schematic phase-space structure for the square cell, in the regions A, B, C and D of figure 4(b). The stable fixed points are shown as solid circles, the sources as open circle and the saddles as crosses. The diagrams represent bidimensional projections in the plane of the in-phase amplitudes. Geometrical relationships are only shown qualitatively. In region A four mixed states and the flat surface are stable. In B only mixed states are stable, as in figure 5. In region C the pure and the mixed states are both stable and eight saddles are interposed between them, as in figure 6. The saddles move from the pure to the mixed-state fixed points as Δ is increased. In region D only the pure states are stable.

the same as it would be for two non-interacting modes; these are the pure states that are shown on the axes of the inner ring in figure 7. The remaining fixed points (mixed-point saddles on the inner ring) must be present for continuity of the differential geometry of the diagram.

In region B only the mixed states are stable. Here the surface is shown as a source, the mixed states are sinks and the pure states are saddles. In region C the mixed modes and the pure modes are sinks while eight saddles are interposed between them. Finally, in region D the pure states of both types are stable, while the mixed states are unstable (saddles).

The multiple bifurcations obtained by varying Δ at fixed frequency are shown schematically in figure 8(a) for negative detuning ($f < 2f_{32} = 2f_{23}$) and in figure 8(b) for positive detuning. The diagrams represent two-dimensional projections, in the space spanned by A_{32} and Δ, of the five-dimensional space spanned by A_{32}, B_{32}, A_{23}, B_{23} and Δ. The various regions in parameter space are schematically marked on the Δ-axis. If the boundary between the flat surface region and region A is crossed (by increasing Δ), pairs of fixed points are generated by bifurcations of the 'saddle node' type, which means that a saddle and a sink (or a saddle and a source) are created

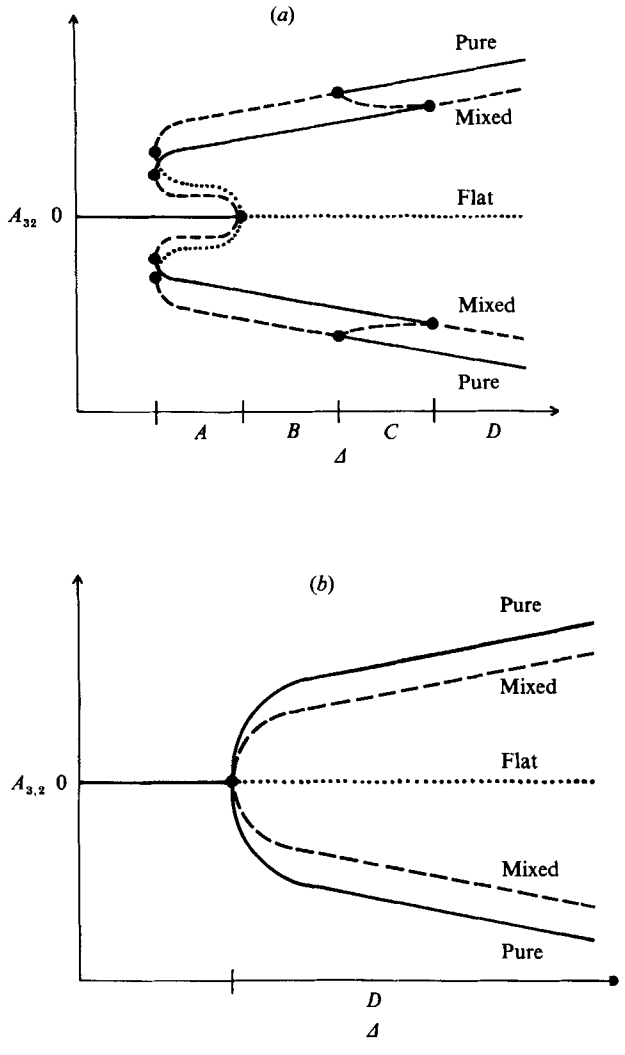

FIGURE 8. Schematic bifurcation diagrams for the square cell. They represent two-dimensional projections of the five-dimensional space spanned by the four mode amplitudes and the driving amplitude Δ. Sinks are represented by solid lines, saddles by dashed lines and sources by dotted lines. (*a*) Bifurcation diagram for increasing Δ with $f < 2f_{32} = 2f_{23}$. The stable mixed states and the unstable pure states (saddles) are first generated by saddle–node bifurcations, together with the unstable points that appear on the inner ring in region A of figure 7. These latter points then merge with the origin at the A–B boundary. The pure-state saddles each later eject two saddles and become sinks at the B–C boundary. Finally, the saddles merge with the mixed-state sinks, which then become unstable. (*b*) Bifurcation diagram for increasing Δ for $f > 2f_{32} = 2f_{23}$. In this case only one bifurcation is encountered. Pure-state sinks and mixed-state saddles are both generated by forward bifurcations.

simultaneously. Using the notation introduced in §3, we summarize this process as follows: $\mathrm{Si} \rightarrow 4(\mathrm{Si^m} + \mathrm{Sa^m}) + 4(\mathrm{Sa^p} + \mathrm{So^p}) + \mathrm{Si}$, where So represents a source, and the other symbols are unchanged. In addition, the superscript p stands for pure states and m stands for mixed states.

When the A–B boundary is crossed, four saddles and four sources merge with the origin, which then becomes a source. (The 'collisions' must happen all at the same

Δ because the stability of the origin cannot be influenced by the nonlinear coupling terms. The linear parts of the amplitude equations are identical for the two modes, so their interchangeability requires that there be only one bifurcation point.) We write this process as $4\mathrm{So}^{\mathrm{p}} + 4\mathrm{Sa}^{\mathrm{m}} + \mathrm{Si} \rightarrow \mathrm{So}$.

At the *B–C* transition each of the pure-mode saddles ejects two saddles and becomes a sink: $4(\mathrm{Sa}^{\mathrm{p}}) \rightarrow 4(\mathrm{Si}^{\mathrm{p}} + 2\mathrm{Sa}^{\mathrm{m}})$. Finally, the saddles ejected from the pure states 'collide' with the mixed states, which then lose their stability and become saddles in region *D*: $4(\mathrm{Si}^{\mathrm{m}} + 2\mathrm{Sa}^{\mathrm{m}}) \rightarrow 4\mathrm{Sa}^{\mathrm{m}}$.

For positive detuning, the situation is much simpler. There is only one bifurcation point where the mixed states (saddles) and the pure states (sinks) are generated from the origin by normal bifurcations, as shown in figure 8(*b*).

6. Interaction of two nearly degenerate modes (rectangular cell)

In order to study the effects of removing the degeneracy, we studied a rectangular cell in which the two modes (3, 2) and (2, 3) are not equivalent. The aspect-ratio of the cell differs from unity by 7%. (The cell size is 6.17×6.6 cm.) This produces a difference of about 1.5% between the resonant frequencies of the two modes. It was not possible to increase this difference without producing unwanted interference from other resonances.

6.1. *Parameter space and bifurcations of fixed points*

A detailed parameter-space diagram for the rectangular cell is shown in figure 9. The entire diagram shows the non-equivalence of the two modes; for example, there is now a region of time dependence located asymmetrically with respect to the two resonances. As noticed for the square cell, this is not surprising since even the single-mode stability diagram is asymmetric with respect to the resonant frequency.

The two resonances are resolved in the rectangular cell; (3, 2) resonates at lower frequency than (2, 3). In regions *B* and *D* of figure 9, only one type of pure state is found. (In each region the mode prevails that is closer to its resonance.) In *C* the two pure states coexist. The flat surface and pure (3, 2) state coexist in *A*, but a similar region for the pure (2, 3) state is not found.

No stable superpositions of the two modes are found for the rectangular cell. On the other hand, time-dependent mixed states are found in *F*. Both time-dependent mixed states and the flat surface are observed in *E*. Finally, the pure (2, 3) state and time-dependent mixed states coexist in region *G*.

The phase-space structure for the time-independent regions was obtained for the rectangular cell and is shown in figure 10. Three stable fixed points, including the origin and two symmetric points representing the pure (3, 2) state, are found in region *A*. The symmetric points differ in phase by π with respect to the forcing. The pure (2, 3) states are saddles. According to the single-mode model discussed in §2.1, there must also be additional (3, 2) and (2, 3) fixed points. A combination of experimental evidence and theoretical argument (similar to that for the square cell) leads us to draw these additional fixed points on an inner ring, as shown.

At the *A–B* transition, the origin loses its stability when the inner sources and saddles coalesce. But this time (in contrast to what happened in the square cell) the coalescence process on the horizontal and vertical axes may not occur at the same Δ. At the *B–C* transition, we find that the pure (2, 3) saddles become sinks by ejecting two saddles each. Finally, upon crossing the *C–D* boundary, the saddles merge with the pure (3, 2) fixed points, causing them to lose their stability.

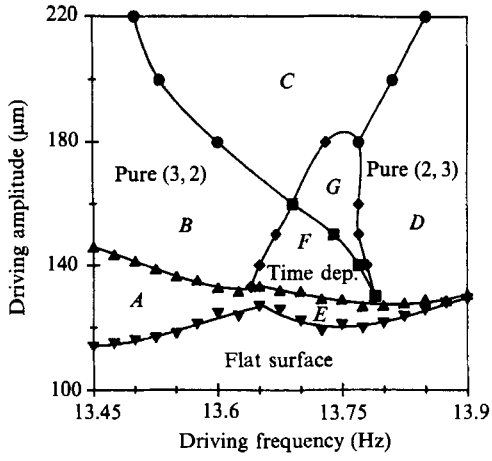

FIGURE 9. Experimental parameter-space diagram for the rectangular cell. The two modes (3, 2) and (2, 3) are resolved; (3, 2) resonates at lower frequency than (2, 3). The fundamental regions are as follows: pure (3, 2) in region B; pure (2, 3) in D, and either periodic or chaotic time dependence in F. In the other regions several solutions coexist: the flat surface and pure (3, 2) states in A, pure (3, 2) and (2, 3) states in C, flat surface chaotic time dependence in E, and finally periodic time dependence and pure (2, 3) in G.

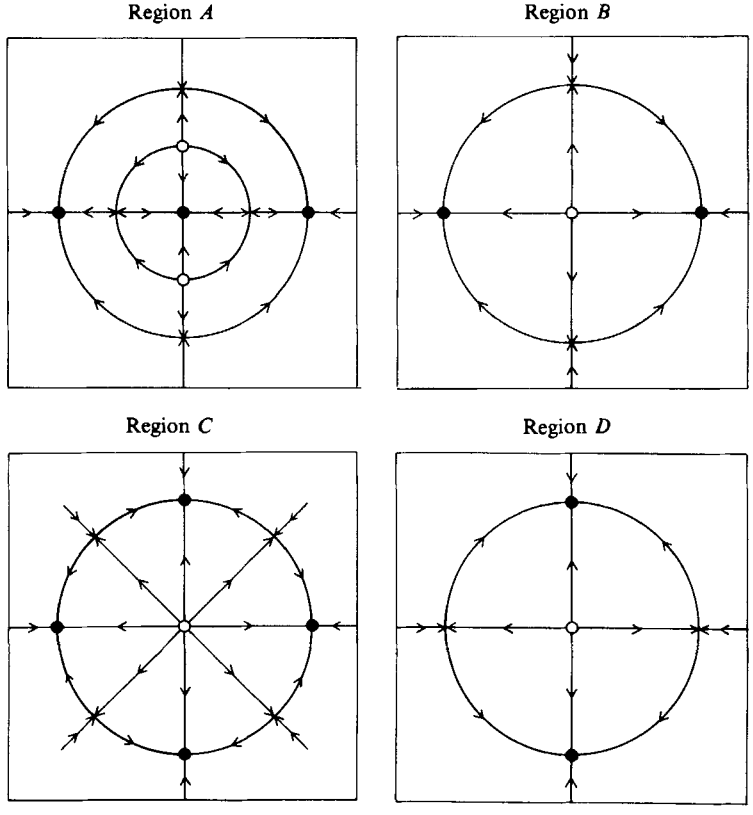

FIGURE 10. Schematic phase-space structures (projected onto the plane of the in-phase amplitudes) in the time-independent regions for the rectangular cell. Symbols are as in figure 7. In region A the (3, 2) states and the origin are stable, while the (2, 3) states are saddles. In B only the (3, 2) states are stable. In C the (2, 3) and (3, 2) states are both stable, and saddles are interposed between them. The saddles originate at the (2, 3) fixed points and move toward the (3, 2) fixed points. In region D the (2, 3) states are sinks while the (3, 2) states are saddles, as a result of the 'collision' with the saddles in C.

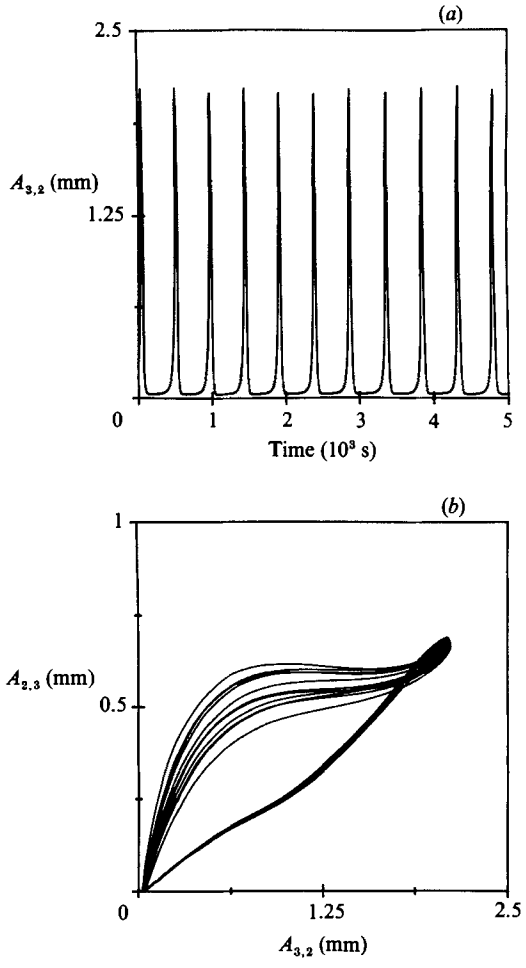

FIGURE 11. Time series (*a*) and phase-space plot (*b*) (in the plane of the in-phase amplitudes) of the periodic spiking process found near the upper boundary of region *E*, figure 9. We observed quiescent periods up to two hours, separated by waves lasting approximately one minute. In this and subsequent figures, the oscillation period may be compared to the (fast) wave period of 0.07 s.

6.2. *Time dependence*

Time dependence in the rectangular cell is organized by simple attractors related to the formerly stable fixed points. In particular, limit cycles centred on mixed states or pure states are found. The time dependence can be either periodic or chaotic, with periodic behaviour being mainly found for higher Δ than chaotic behaviour.

When Δ is increased very slowly to enter the time-dependent region, the first state encountered is a periodic relaxation oscillation. The surface stays flat for a considerable time, then a large wave (several mm in height) grows, reaches a maximum, and decays, all in a time short compared with the period. This oscillation is shown in figure 11 in the time domain and in phase space.

The wave that develops during the spike can be either a mixed or a pure state, depending on the driving frequency. The duration of the spikes is practically independent of Δ, while the period of the oscillation changes dramatically with Δ, appearing to diverge at the lower boundary Δ_c of region *F*. The form of this

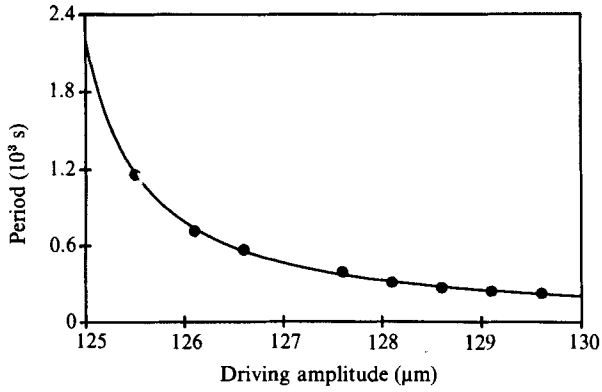

FIGURE 12. Period of the oscillation in figure 11 as a function of the driving amplitude. The data are obtained at a driving frequency of 13.8 Hz and are compared to a function $T = T_0[\Delta_c/(\Delta-\Delta_c)]^\alpha$. The best fitting exponent is $\alpha = 1.1^{+0.15}_{-0.03}$.

divergence is explored in figure 12, where the experimental data are compared to a fitted power law of the following form:

$$T = T_0[\Delta_c/(\Delta-\Delta_c)]^\alpha. \tag{6.1}$$

This function contains three adjustable parameters: T_0, Δ_c and α. We find an adequate fit, and the best fitting exponent α is $1.1^{+0.15}_{-0.03}$. (The error is computed from the shape of the χ^2 function near its minimum.)

If Δ is further increased, the system jumps discontinuously to a chaotic attractor centred on a mixed mode. Because of this discontinuity, it is more natural to study the transition to chaos for decreasing Δ. A typical sequence of phase-space plots and time series is shown in the figures 13–15. The driving frequency is 13.75 Hz in all cases and the values of Δ are noted on the figures.

The first state shown (near the upper boundary of region F in figure 9) is a nearly sinusoidal oscillation at 13 mHz that is stable over a large range in Δ ($145 < \Delta < 180$ μm). In phase space the attractor is arc-shaped and centred on the pure (3,2) mode; two projections are shown in figure 13, one in the subspace spanned by A_{32}, A_{23} and another in the subspace spanned by A_{23}, B_{23}.

As Δ is reduced, the attractor develops additional loops, via bifurcations that break and then restore the symmetry of the attractor by adding loops on alternate sides. (The symmetry is always approximate, perhaps due to small experimental errors in the mode decomposition process.) The bifurcations become more closely spaced as the sequence progress, and only the first few are actually resolved. A series of those attractors for decreasing Δ is shown in the time domain and in phase space in figure 14. Beyond a certain point (see figures 14i,j) the attractor becomes extremely asymmetric. The system now spends most of its time on one side of the attractor until the arc shape is completely lost and a chaotic attractor is established, this time centred on a mixed mode (figure 15). This attractor was identified as chaotic by standard tests (Swinney & Gollub 1986), but a detailed study of its geometry is outside of the scope of this paper. That attractor persists for decreasing Δ through region E of figure 9 until, with a sharp transition, the surface becomes flat again. Note that this chaotic attractor and the relaxation oscillation overlap in Δ, so that both are present (for different initial conditions) in a small interval at the lower edge of region F of figure 9.

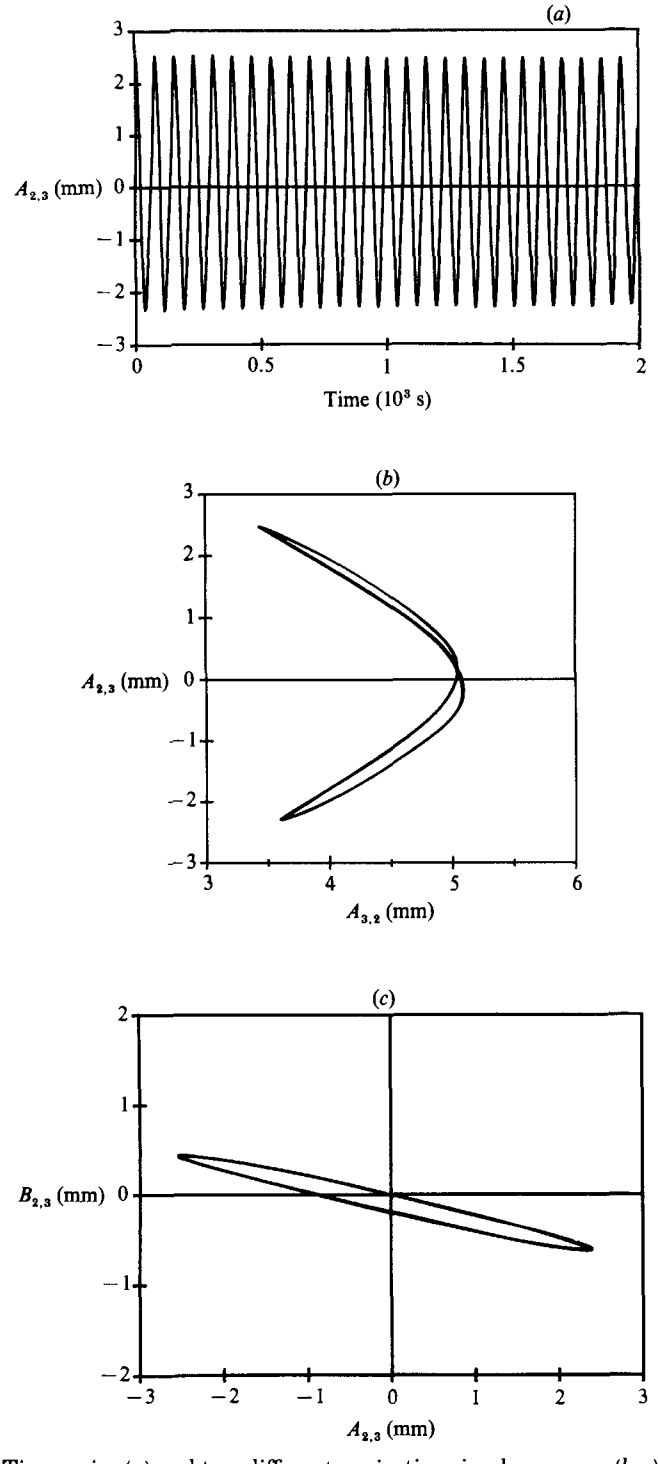

FIGURE 13. Time series (*a*) and two different projections in phase space (*b*, *c*) for the oscillating state whose transition to chaos was studied in detail. Here, $f = 13.75$ Hz, $\Delta = 150.4$ μm, and the oscillation frequency is 13 mHz. From the phase portraits it is clear that the arch-like attractor is centred on a pure (3, 2) state. This periodic state is found for $145 < \Delta < 180$ μm at this driving frequency and for similarly large intervals for other driving frequencies.

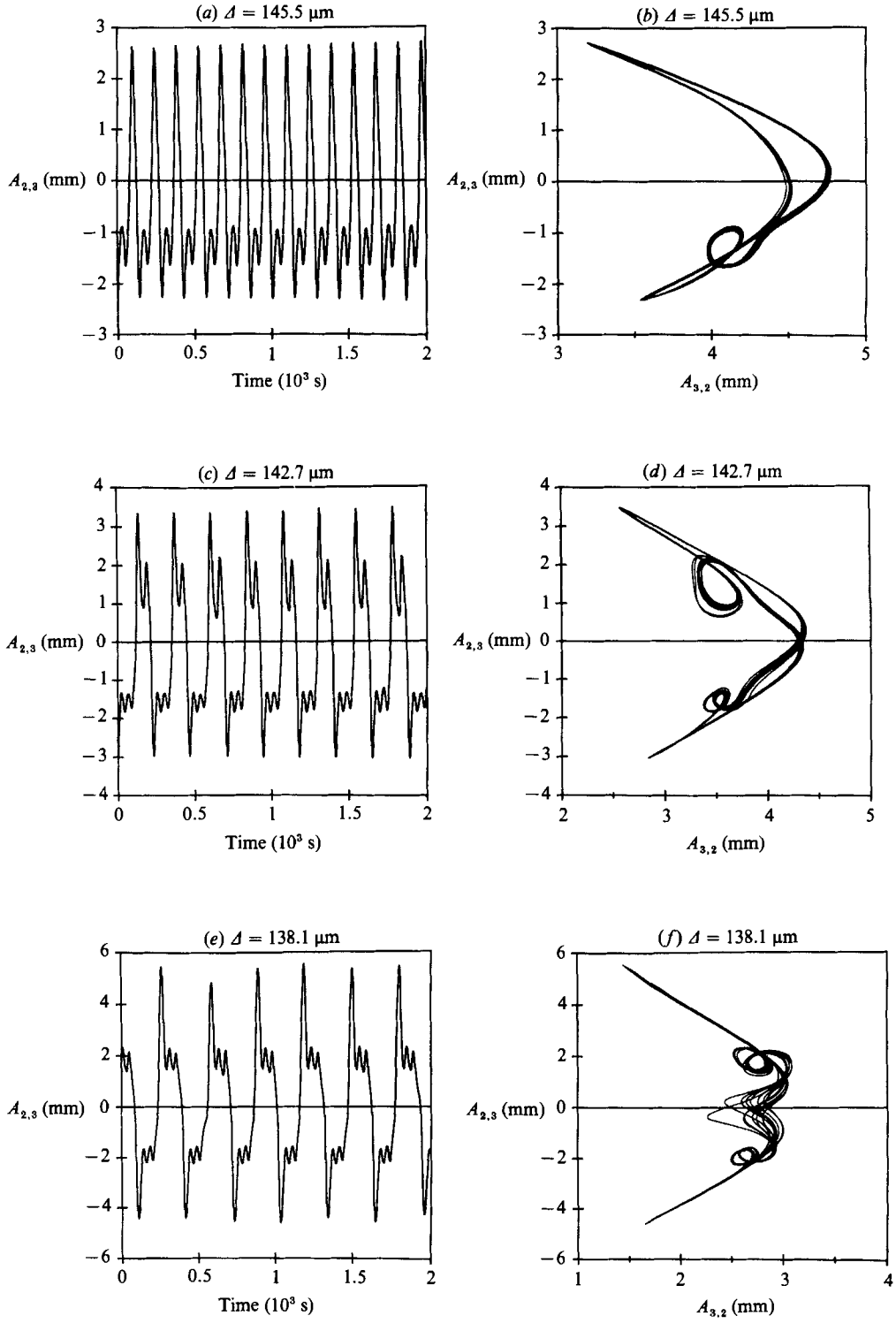

FIGURE 14(a–f). For caption see facing page.

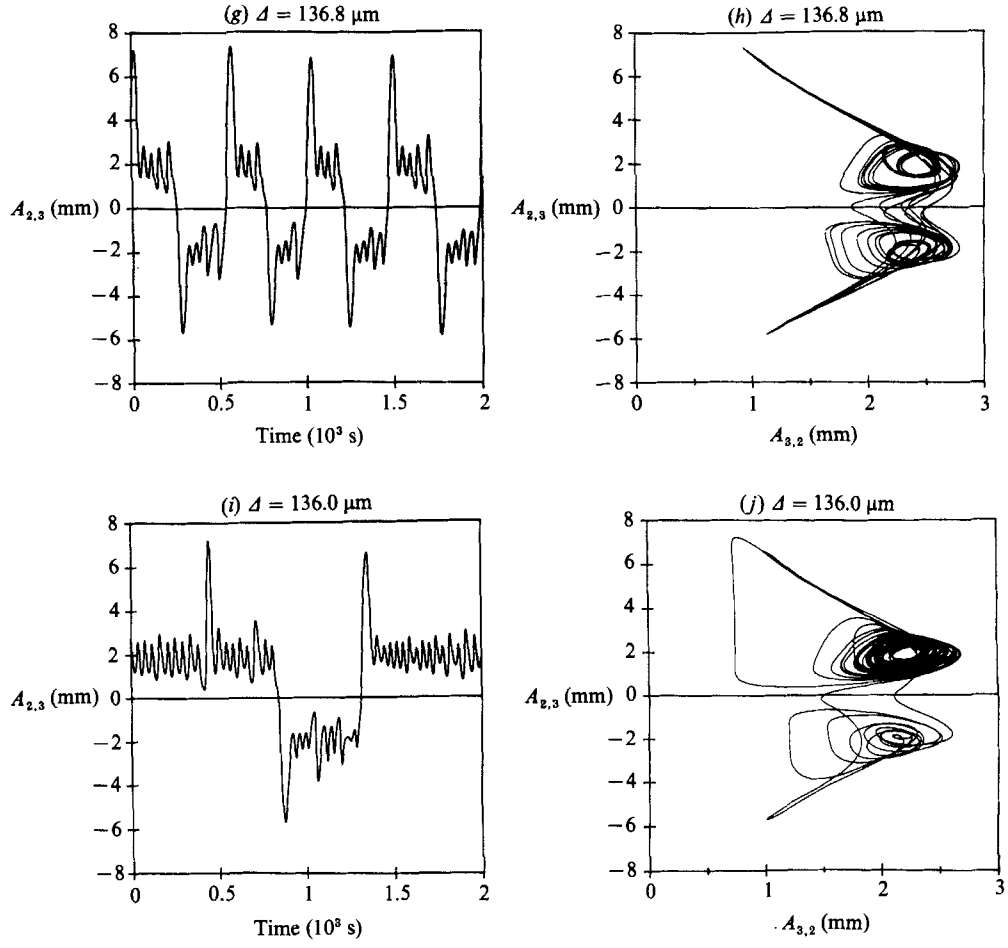

FIGURE 14. Sequence of time-series and phase-space plots for decreasing values of Δ (as indicated on the individual plots) at $f = 13.75$ Hz. The sequence $(a$–$h)$ shows how the attractor becomes more and more complicated by the addition of loops on alternate sides. With a further decrease of Δ the attractor becomes strongly asymmetric (i, j) until a chaotic attractor centred on a mixed mode is established (see figure 15).

7. Discussion

7.1. *Consequences of symmetry breaking*

The dramatic effects of removing the degeneracy of the two interacting modes by breaking the geometrical symmetry have been documented in this experiment. It is natural then to ask what degree of asymmetry is required to produce these effects. We found that a detuning of the two modes by only 0.5%, one third that of figure 9, produced essentially the same effects. Furthermore, even the nominally square cell showed a striking sensitivity to small (uncontrollable) perturbations (Simonelli & Gollub 1987). For example, when the square cell was repeatedly cleaned and refilled, a region of slow time dependence was found in several runs, though robust and repeatedly time dependence was found only for the rectangular cell.

In figure 16 we show an example of time-dependent phenomena for a nominally square cell. Two different attractors are reached for different initial conditions close to the origin. In one case a periodic limit cycle is established after a few oscillations.

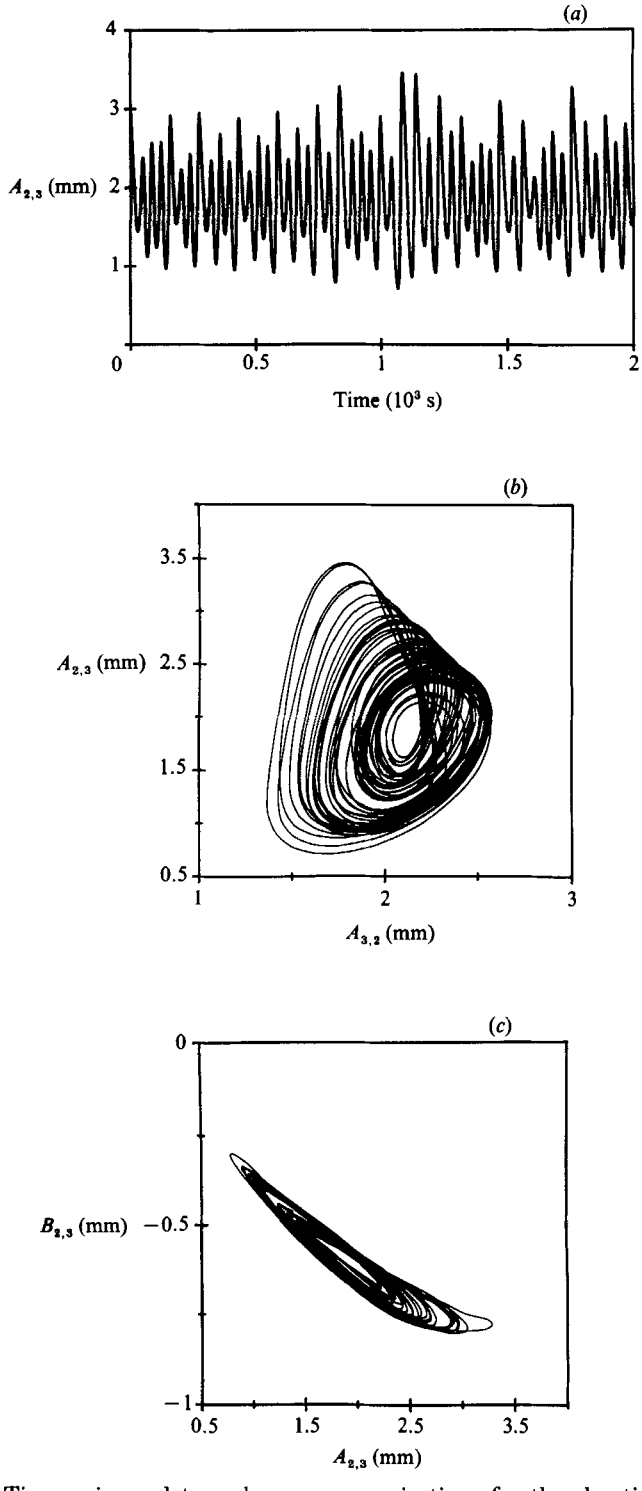

FIGURE 15. Time-series and two phase-space projections for the chaotic attractor centred on a mixed mode. This state is first observed at $\Delta = 135.2$ when $f = 13.75$ Hz, and is maintained for smaller Δ until the system jumps discontinuously to the flat-surface state at the lower boundary of region E of figure 9.

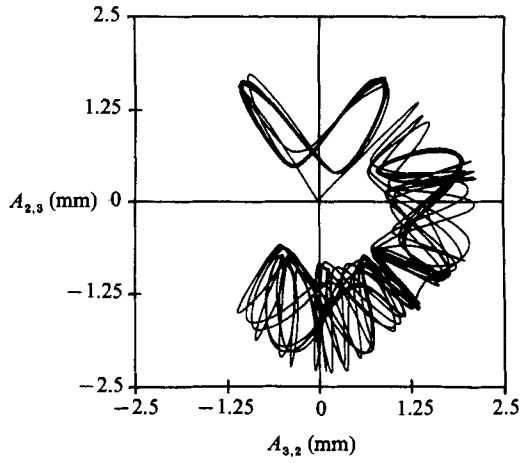

FIGURE 16. Example of time dependence found occasionally in the square cell. The data are obtained at $f = 14.1$ Hz and $\Delta = 161$ μm. A limit cycle and a chaotic attractor are reached for two different initial conditions. Typical timescales of oscillations are longer than in the rectangular cell by a factor of four. We interpret this non-reproducible slow time dependence as evidence for a lack of structural stability (i.e. sensitivity to perturbances) of the square-cell dynamics.

In the other the system wanders in an irregular way, visiting a large portion of the phase space. In some runs we observed very long and complicated transients lasting for several hours, times that are approximately two orders of magnitude longer than the typical timescale for modal interaction shown in figure 13 (Simonelli & Gollub 1987).

We infer from these observations that the degenerate case may be structurally unstable (Guckenheimer & Holmes 1983) with respect to small symmetry-breaking perturbations, in the sense that a very small asymmetry is sufficient to produce a qualitative change in the dynamics. Since in most cases we did not observe time-dependent states in the square cell, we concluded that time dependence near onset in that geometry is non-generic and hence did not study it further.

Though the consequences of symmetry breaking are dramatic, it was not possible to determine experimentally how the system goes from the parameter space of figure 4(*b*) to that of figure 9 as the internal detuning is increased. This is a fascinating question for theoretical consideration.

7.2. *Comparison with theory for the square cell*

For the square case, symmetry requirements leave a relatively small number of distinct free parameters (five complex coefficients) in the amplitude equations (2.3). J. Guckenheimer (1988, private communication) suggested that it might be possible to fit the model to the experimental data, and has attempted to do so. It is in fact possible to reproduce the qualitative structure of the parameter space of figure 4(*b*) (including the intersection of the four stability boundaries at the resonance) and the general topology of the phase diagrams (figure 7) and bifurcation sequences (figure 8), provided that the coefficients of the nonlinear terms are purely imaginary. It can be shown that this implies the system of equations to be Hamiltonian in the absence of damping; the latter enters through the real part of the coefficient α in (2.2) (Meron 1987). In addition, no Hopf bifurcations will occur if the coefficients are such that the system (without damping) is Hamiltonian. This absence of Hopf bifurcations is

consistent with the observations, again supporting the Hamiltonian character of the underlying dynamics.

Thus, the behaviour of the square cell can be qualitatively described by the third-order amplitude equations, with suitable coefficients. However, efforts to obtain a quantitative fit to figure 4(*b*) were unsuccessful, because the model does not allow stability boundaries with negative curvature (i.e. that are concave downwards). This failure suggests that it may be necessary to include certain fifth-order terms to describe the parameter space quantitatively. The need for higher-order terms seems plausible in view of the following fact: if the model is rewritten in terms of the moduli of the complex amplitudes, then the coefficients of the cubic terms pass through zero at the resonance, where the bifurcation changes from subcritical to supercritical. It is apparent that additional attention to this problem from the standpoint of bifurcation theory would be useful. Some possibly relevant analysis appropriate for the centre manifold of a square cell has been done by Golubitsky & Roberts (1987) and Crawford & Knobloch (1988).

During the preparation of this manuscript, the authors became aware of simultaneous work by Feng & Sethna (1989) based on perturbation expansions of the full hydrodynamic equations. They obtain equations identical in form to (2.3) by direct computation instead of symmetry requirements. Furthermore, they determine expressions for the coefficients, and work out the resulting bifurcation sequences in some detail. Our experimental work seems to be in qualitative agreement with their predictions. However, some differences are found. In particularly they describe (and have observed) two distinct types of stable mixed states, only one of which is seen in the present investigation. We find that the phases of the modes in the mixed states are equal in some cases and differ by π in others. Feng & Sethna also describe stable mixed states in which the two modes differ in phase by $\frac{1}{2}\pi$, and hence the pattern appears to rotate at $\frac{1}{2}f$. Detailed comparison of the results of these two investigations is an interesting topic for future work.

7.3. *Time-dependent phenomena*

Though the time-dependent states in the rectangular cell are essentially not understood at the present time, the role of the pure- and mixed-mode fixed points in organizing the time-dependent phenomena is clearly evident. Also, the periodic spiking was identified as a heteroclinic loop passing near unstable fixed points.

The route to chaos found experimentally can possibly be described, in its first steps, by means of 'symbolic dynamics'. Referring to the phase space plots showing projections in the subspace A_{32}, A_{23}, we can assign a symbol P to the loops with positive A_{23} and N to the loops with negative A_{23}. In this notation, we can describe figure 13 as (PN), figure 14(*a*, *b*) as (PNN), figure 14(*c*, *d*) as (PPNNN), and figure 14(*e*, *f*) as (PPPNNN). We believe that the state (PPNN) may be present but unresolved. These identifications may also be made from the numbers of positive and negative peaks in the time series. Meron & Procaccia (1987) and Meron (1987) made interesting predictions about the routes to chaos in interacting surface waves and in parametrically forced systems in general. They observe numerically a route to chaos via a well-defined sequence of bifurcations to states of increasingly complex symbol sequences. The sequences observed in our experiments resemble in some respects those found numerically, but appear to differ from them in detail.

7.4. *Remarks on the experimental approach*

The phenomena investigated in this paper could not have been studied without the experimental methods described above. The modal decomposition process clearly revealed the physical nature of the various pure and mixed states. Automation of the process of finding stability boundaries was necessary in order to explore the phenomena as a function of two external parameters in a reasonable time. Finally, the use of repetitive transients to study the phase-space structure and locate unstable fixed points was critical in determining the bifurcation sequences. Once the need for these methods was recognized, they were not particularly difficult to implement, and may prove useful elsewhere as well. It would be interesting to extend the use of repetitive transients to the time-dependent regime, in order to investigate the evolution of unstable orbits and their interactions with attractors. Similarly, the method of determining stability boundaries could be extended to the study of boundaries separating distinct types of time-dependent states.

We appreciate helpful discussions and an exchange of preliminary results with J. Guckenheimer and P. R. Sethna. We also have benefited from discussions with M. Golubitsky and E. Meron. This work was supported by the DARPA Applied and Computational Mathematics Program through the University Research Initiative Program, Contract Number N00014-85-K-0759 to Princeton University.

Note Added in Proof. A theoretical description of the behaviour observed for the square cell has been proposed by Silber & Knobloch (1988) using a two-dimensional map that is equivariant with respect to the symmetry group D_4.

REFERENCES

Ciliberto, S. & Gollub, J. P. 1984 Pattern competition leads to chaos. *Phys. Rev. Lett.* **52**, 922–925.

Ciliberto, S. & Gollub, J. P. 1985*a* Chaotic mode competition in parametrically forced surface waves. *J. Fluid Mech.* **158**, 381–398.

Ciliberto, S. & Gollub, J. P. 1985*b* Phenomenological model of chaotic mode competition in surface waves. *Il Nuovo Cimento* **6**, 309–316.

Crawford, J. & Knobloch, E. 1988 Classification and unfolding of degenerate Hopf bifurcations with O(2) symmetry: no distinguished parameter. *Physica* D **31**, 1–48.

Feng, Z. C. & Sethna, P. R. 1989 Symmetry-breaking bifurcations in resonant surface waves. *J. Fluid Mech.* **199**, 495–518.

Funakoshi, M. & Inque, S. 1987 Chaotic behaviour of resonantly forced surface waves. *Phys. Lett.* A **121**, 229–232.

Golubitsky, M. & Roberts, M. 1987 A classification of degenerate Hopf bifurcation with O(2) symmetry. *J. Diffl. Equat.* **69**, 216–264.

Golubitsky, M. & Shaeffer, D. G. 1985 *Singularities and Groups in Bifurcation Theory.* Springer.

Gu, X. M., Sethna, P. R. & Narain, A. 1988 On three-dimensional non-linear subharmonic resonant surface waves in a fluid. Part I: Theory. *Trans. ASME* E: *J. Appl. Mech.* **55**, 213–219.

Gu, X. M. & Sethna, P. R. 1987 Resonant surface waves and chaotic phenomena. *J. Fluid Mech.* **183**, 543–565.

Guckenheimer, J. & Holmes, P. 1983 *Nonlinear Oscillations, Dynamical Systems and Bifurcation of Vector Fields.* Springer.

HOLMES, P. J. 1986 Chaotic motion in a weakly nonlinear model for surface waves. *J. Fluid Mech.* **162**, 365–388.

MERON, E. 1987 Parametric excitation of multimode dissipative systems. *Phys Rev.* A **35**, 4892–4895.

MERON, E. & PROCACCIA, I. 1986*a* Theory of chaos in surface waves: The reduction from hydrodynamics to few-dimensional dynamics. *Phys Rev. Lett.* **56**, 1323–1326.

MERON, E. & PROCACCIA, I. 1986*b* Low dimensional chaos in surface waves: Theoretical analysis of an experiment. *Phys. Rev.* A **34**, 3221–3237.

MERON, E. & PROCACCIA, I. 1987 Gluing bifurcations in critical flows: The route to chaos in parametrically excited surface waves. *Phys. Rev.* A **35**, 4008–4011.

MILES, J. W. 1967 Surface wave damping in closed basins. *Proc. R. Soc. Lond.* A **297**, 459–475.

MILES, J. W. 1976 Nonlinear surface waves in closed basins. *J. Fluid Mech.* **75**, 419–448.

MILES, J. W. 1984*a* Nonlinear Faraday resonance. *J. Fluid Mech.* **146**, 285–302.

MILES, J. W. 1984*b* Resonantly forced surface waves in a circular cylinder. *J. Fluid Mech.* **149**, 15–31.

SILBER, M. & KNOBLOCH, E. 1988 Parametrically excited surface waves in square geometry. (submitted to *Phys. Lett.*).

SIMONELLI, F. & GOLLUB, J. P. 1987 The masking of symmetry by degeneracy in the dynamics of interacting modes. *Nuc. Phys. B (Proc. Suppl.)* **2**, 87–96.

SIMONELLI, F. & GOLLUB, J. P. 1988 Stability boundaries and phase space measurements for spatially extended dynamical systems. *Rev. Sci. Instrum.* **59**, 280–284.

SWINNEY, H. L. & GOLLUB, J. P. 1986 Characterization of hydrodynamic strange attractors. *Physica* **18 D**, 448–454.

VIRNIG, J. C., BERMAN, A. S. & SETHNA, P. R. 1988 On three-dimensional non-linear subharmonic resonant surface waves in a fluid. Part II: Experiment. *Trans. ASME* E: *J. Appl. Mech.* **55**, 220–224.